Extreme low-level wind jets in Storm Ciarán

Gray, S. L. ORCID: https://orcid.org/0000-0001-8658-362X and Volonté, A. ORCID: https://orcid.org/0000-0003-0278-952X (2024) Extreme low-level wind jets in Storm Ciarán. Weather. ISSN 1477-8696 doi: 10.1002/wea.7620 Available at https://centaur.reading.ac.uk/118694/

Extreme low-level wind jets in Storm *Ciarán*

Suzanne L. Gray[1] (ID) **and Ambrogio Volonté[1,2]** (ID)

[1] Department of Meteorology, University of Reading, UK

[2] National Centre for Atmospheric Science, University of Reading, UK

Introduction

While there are three main, relatively long-lived, airstreams with the potential to lead to strong near surface winds and gusts in extratropical cyclones, the smaller scale transient 'sting jet' has captured media attention due to its potential to bring the strongest winds and exceptionally strong gusts, in some of the most impactful storms. Here we investigate the cause of the strong surface winds and gusts in Storm *Ciarán*, the synoptic scale structure of which was well forecast by both machine learning and numerical weather prediction models (Charlton-Perez *et al.*, 2024). The typical paths of cyclone airstreams are marked on the satellite image of Storm *Ciarán* in Figure 1(a). The sting jet is an airstream that descends from mid-tropospheric levels inside the cloud head into the frontal fracture region

of a cyclone developing following the 'Shapiro–Keyser' conceptual model (Shapiro and Keyser, 1990) over a period of a few hours leading to a distinct region of near-surface stronger winds, perhaps 50–100km across (as defined in the review by Clark and Gray (2018)). Shapiro–Keyser cyclones are distinct from cyclones evolving following the classical Norwegian model (the other main conceptual model of extratropical cyclone development) because they feature frontal development with a 'T-bone' structure, that is, a right angle between the cold and warm fronts and a region of weak horizontal temperature gradients in the part of the cold front closest to the cyclone centre (the frontal fracture). These weak temperature gradients are argued to be necessary for the sting jet to descend. The sting jet is distinct from the other main cyclone airstreams (the warm and cold conveyor belt jets and the dry intrusion) although it is usually not possible to confidently identify the sting jet from surface observations alone as the cold conveyor belt jet and dry intrusion can also lead to strong winds in the same part of the storm, typically to the southwest or south (in the Northern Hemisphere) of the low-pressure centre.

While the motivation for this study is the possible existence of a sting jet, a

brief description of these other airstreams is needed to distinguish it from them (see Browning and Roberts (1994) for a fuller description of these airstreams). The warm conveyor belt is typically the main precipitation producing airstream and ascends poleward from the warm sector of storms, ahead of the surface cold front. It can split into cyclonically and anticyclonically turning branches as it ascends, with the cyclonically turning branch travelling poleward of the low-pressure centre to form the upper part of the hooked cloud head. The cold conveyor belt travels mainly rearward relative to the motion of the stormahead beneath the sloping warm front on the poleward side of the low-pressure centre; it forms the lower part of the cloud head and the associated jet can lead to strong near-surface winds as it hooks completely around the storm centre in mature storms to have a wind component that aligns with the storm motion vector. Finally, the dry intrusion descends from the upper-troposphere to the rear of the storm towards the cold front. If it overruns the cold front it can create convective destabilisation as the dry air overruns the moist surface layer. Surface wind gusts can occur directly due to the convection (i.e. due to convective downdraughts) or due to

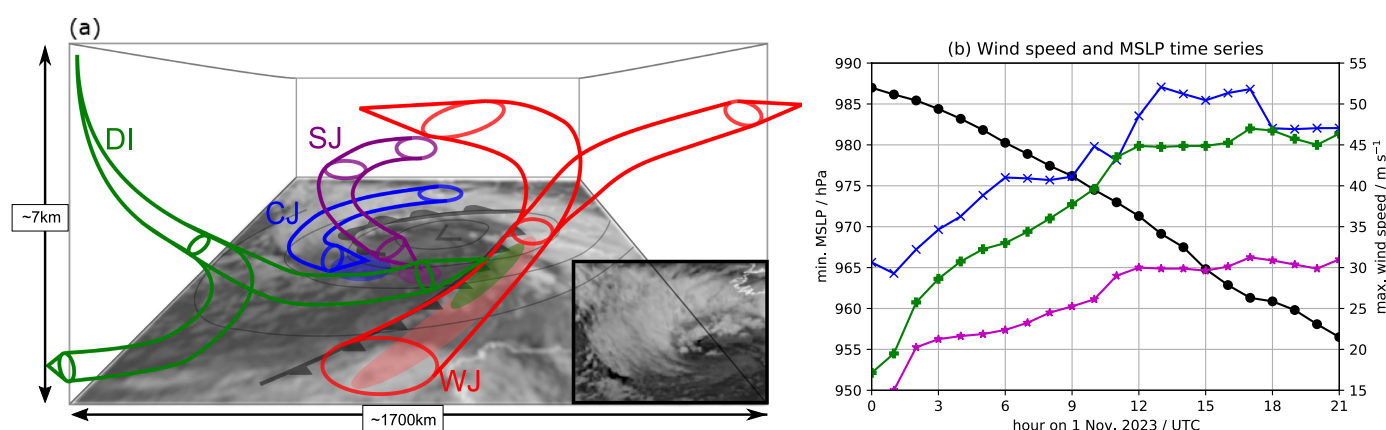

Figure 1. Evidence of possible sting jets in Storm Ciarán. *(a) Schematic showing the three-dimensional airstreams that can cause strong near-surface winds in cyclones developing according to the Shapiro–Keyser conceptual model of cyclone evolution (in the Northern Hemisphere). The airstreams corresponding to the warm and cold conveyor belt jets (WJ and CJ, respectively), the sting jet (SJ) and the dry intrusion (DI) are shown by open arrows with the corresponding surface footprint indicated by an ellipse in the same colour. Mean sea-level isobars (surrounding the low-pressure centre marked by 'L') and surface fronts are indicated in grey by contours and conventional frontal symbols, respectively. Infrared (10.8μm) satellite imagery showing the cloud structure of Storm Ciarán as it approaches western Europe is underlain with the cloud head banding revealed in the inset cutout of the imagery which shows the cloud head tip (some editing has been applied to enhance these images). The image is a high Rate SEVIRI image from the Meteosat second-generation 0 degree satellite taken at 1700 UTC on 1 November 2023 ©EUMETSAT [2023]. (b) Time-series of maximum 850hPa windspeed (blue with crosses), 10m windspeed (magenta with stars) and 10m gusts (green with pluses) in the cold sector, and minimum MSLP (black with circles) during 1 November 2023 from the Met Office global operational forecast initialised at 0000 UTC on the same day where the cold sector is defined as where 850hPa θ_w < 286K and within −2.5° to 0.5° in latitude and −5° to 1° in longitude of the diagnosed MSLP centre. Schematic adapted from Clark and Gray (2018) to include the DI and satellite imagery.*

downward momentum transport from the dry intrusion (e.g. as described in Browning and Reynolds (1994)).

Figure 1(a) also shows characteristic narrow cloud bands (or 'fingers') at the tip of *Ciarán*'s cloud head as it hooks around the low-pressure centre (see inset). As the sting jet(s) descend from the cloud head tip, evaporation occurs leading to these bands of drier air which can be very clear in satellite infrared or water vapour imagery. This feature is often used as a way of nowcasting (producing a very short forecast for the next few hours) that a sting jet is occurring. These bands have often been observed in extreme windstorms for which later, detailed analysis has proven sting jet existence; however, as yet, no systematic assessment has been performed of the relationship between observed bands and sting jets causing enhanced near-surface winds.

Here we use output from a Met Office operational global model forecast (starting at 0000 UTC on 1 November) to demonstrate the existence of sting jets, together with the overrunning dry intrusion, in Storm *Ciarán* and present the characteristics of these airstreams. This model has been used previously for analysis of sting jet storms (e.g. Martínez-Alvarado *et al.*, 2014; Volonté *et al.*, 2024a,b). With ≈10km horizontal grid spacing in the mid-latitudes (N1280, equal to 2560 longitude points and 1920 latitude points) and 70 levels up to a lid at about 80km, it is capable of representing synoptic-scale features well and mesoscale features such as sting jets partially (as their representation is potentially somewhat limited by the vertical resolution; the mid-tropospheric level spacing is about 300m at 3km).

The three-dimensional structure of the low-level jets

Storm *Ciarán* was an extratropical cyclone 'bomb' (Sanders and Gyakum, 1980) and deepened rapidly as it crossed the North Atlantic towards the UK, with the minimum mean sea-level pressure (MSLP) dropping from 987 to 957hPa from 0000 to 2100 UTC on 1 November (Figure 1b) and reaching a minimum of 953hPa (according to the 6-hourly Met Office analysis charts) at 0600 UTC 2 November, with the 953.3hPa observed at Plymouth setting a new November record for southern England (Kendon, 2023). As expected, the deepening storm was associated with strengthening maximum wind speeds. Here we focus on the wind speeds in the cold sector of *Ciarán* (in the frontal fracture region and behind the surface cold front), as this is where sting jets can descend towards the surface. The maximum values of the winds here at 850hPa (a pressure level about 1–1.5km above the surface and typically near the top of the atmospheric boundary layer)

and winds and gusts at 10m (the height at which synoptic surface wind observations are reported) are also shown in Figure 1(b). The winds at 850hPa are much stronger than those at 10m due to the much reduced surface friction at this level, but the 10m gusts approach the values of the 850hPa winds (indeed the 850hPa wind speed is sometimes used as a proxy for 10m gusts, as justified in Sect. 2(d) of Hart *et al.* (2017)). Three clear short-lived peaks in 850hPa wind speed occurred at 1000, 1300 and 1700 UTC with the last of these also associated with a peak in 10m winds and gusts. According to the Beaufort scale, sustained winds (wind speed averaged over a period of 10min) of 30ms^{-1} (the approximate value of the 10m wind speed in Figure 1(b) between 1200 and 2100 UTC) equate to a 'violent storm' (Beaufort force 11), with sea covered in white foam, visibility seriously affected and estimated probable wave heights of 11.5m in open seas (Met Office, 2024). We hypothesise that the last two 850hPa wind speed peaks are associated with the descent of sting jets towards the top of the boundary layer where they can then enhance surface winds through downward transport of the associated momentum to the surface through convective rolls or turbulent mixing (as demonstrated in the idealised simulations in Rivière *et al.* (2020)); the first, weaker peak at 1000 UTC is associated with the warm

conveyor belt jet, but identified erroneously as being in the cold sector due to distortions in the wet bulb potential temperature (θ_w) surfaces in the warm sector at this time (not shown). Hereafter we focus on the times of the strongest of 850hPa wind speed peaks: 1300 and 1700 UTC.

The structure of the wind field in Storm *Ciarán* at 1300 UTC is illustrated in Figure 2 by maps of the winds at 700hPa, 850hPa and 10m, and a vertical cross section through the region of strongest cold-sector winds shown in the maps; the location of the low-pressure centre can be identified from the MSLP contours, the surface fronts are indicated by three contours of 850hPa θ_w, chosen to highlight the strongest gradients and frontal-fracture region, and the mid-tropospheric cloud is indicated by the stippled regions. Two distinct wind maxima exist at 850hPa (Figure 2b), one ahead of and aligned with the cold front with winds up to 45–50ms^{-1} (the expected location of the warm conveyor belt jet) and another more compact and stronger maximum, exceeding 50ms^{-1}, in the cold air near the tip of the bent-back warm front and in the frontal fracture region (the hypothesised sting jet). Slightly higher up in the troposphere, at 700hPa, the wind structure is rather different with the peak winds (also exceeding 50ms^{-1}) found in a wide band lying along and immediately behind
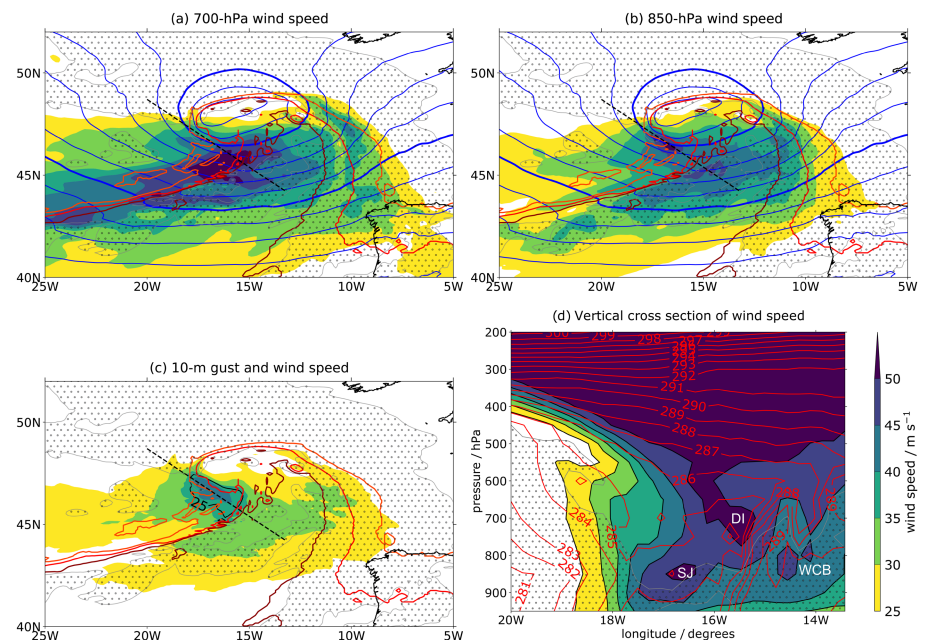

Figure 2. Three-dimensional structure of Storm Ciarán *at 1300 UTC 1 November illustrated by (a–c) horizontal maps at different levels and (d) a vertical cross section from (20°W, 48.7°N)–(13.2°W, 44.2°N); the location of this cross section is marked in panels (a–c). Colour shading shows, using the same scale for all panels, (a) 700hPa wind speed, (b) 850hPa wind speed, (c) 10m gusts and (d) wind speed interpolated onto the cross section. In (c) the 10m wind speed is shown by a black contour for 25ms^{-1} (speed does not reach 30ms^{-1}). MSLP (blue contours every 4hPa with thick contours for 1000 and 980hPa), 850hPa θ_w (contours at 284, 286 and 288K in orange to red chosen to show the position of the tight frontal thermal gradient and frontal-fracture region) and 700hPa cloud (stippling shows relative humidity with respect to ice exceeding 90%) are overlain in (a–c). Cloud and θ_w (contours every 1K) are also overlain in (d). The locations of the inferred sting jet (SJ), dry intrusion (DI) and warm conveyor belt jet (WCB) are indicated in (d).*

RMetS
Royal Meteorological Society

the surface cold front, although localised regions of stronger winds are also still visible in the regions where they are found at 850hPa; this 700hPa wind band will be shown to result from the dry intrusion. The locations of strongest winds (contoured) and gusts (shaded) at 10m resemble those at 850hPa, albeit with much weaker values (Figure 2c). The peak wind speeds (of up to 25–30ms^{-1}) are found in the cold sector and frontal fracture region directly beneath the wind maximum hypothesised to be due to the sting jet, as are the peak gusts (of up to 40–45ms^{-1}). The ratio between the peak gusts in the cold and warm sectors is higher than that between the 850hPa winds in the corresponding regions. Cyclone warm sectors typically have a shallow stable atmospheric boundary layer, whereas the cold sector boundary layer is often deeper and more unstable due to the passage of cold air over the relatively warm ocean surface leading to sensible and latent heat fluxes from the ocean surface into the boundary layer. Hence, there is typically greater mixing of air with large values of momentum downward towards the surface through convective destabilisation in the cold sector (e.g. see table 2 of Hewson and Neu, 2015). The equivalent figure to Figure 2 for 1700 UTC shows the same main features (not shown).

The distinct nature of the different wind jets is evidenced by the vertical cross section through the region of the hypothesised sting jet (Figure 2d extending from the west to southeast of the cyclone centre). The hypothesised sting jet can be seen peaking at over 50ms^{-1} between 800 and 900hPa in non-cloudy air above a shallow moist zone. The peak winds are in a region of very slack horizontal and vertical θ_w gradients, behind a narrow region with a strong horizontal θ_w gradient sloping forward from the surface associated with the cold front and ahead of an extended region of weaker low-level horizontal θ_w gradient where the section cuts through the tip of the bent-back front at a shallow angle. Ahead of the surface cold front there is some evidence of the warm conveyor belt jet with a small region exceeding 45ms^{-1} at 800hPa in cloudy air. Between and above these two maxima in non-cloudy air lies another strong wind region that appears, in this section at least, to extend downwards in a filament from the upper troposphere. This is the northern part of the wide band of 700hPa peak winds lying behind and along the cold front in Figure 2(a), which is hypothesised to be due to the dry intrusion. Finally, there is no evidence of a distinct wind maximum associated with the cold conveyor belt jet in Figure 2. Analysis of similar plots at later times (not shown) reveal that this jet begins to appear as a distinct wind maximum at 2100 UTC behind the, now far weaker, wind region associated with the sting jet.

An alternative view of *Ciarán*'s wind structure is shown using three-dimensional rendering in Figure 3. Viewed from the north (Figure 3a) the 50ms^{-1} isosurface enveloping the strongest winds can be seen extending across the domain from west to east: this is the upper tropospheric jet. The base of the jet is distorted above *Ciarán*'s MSLP centre with filaments descending downwards (forming the dry intrusion jet). The lowest region of strong winds, the hypothesised sting jet, is a small separate blob that lies directly above the region of peak 10m wind gusts. Figure 3(b) provides an alternative view of *Ciarán* from the northeast at the same time. The sting jet blob is again seen to be separate from the upper-tropospheric jet and also shown to lie ahead of a 'valley' (marked by a dashed line) in the isosurface of θ_w also shown in this panel; this valley implies the existence of a narrow wedge of higher θ_w values. A similar deformation of a θ_w isosurface was also found for windstorm *Tini* (see fig. 15 of Volonté *et al.*, 2018) where the locations of sting jet trajectories intersecting the isosurface clearly revealed that the localised folding was closely associated with the rapid descent of the sting jet into the frontal fracture region.

Lagrangian trajectory analysis

While the three-dimensional analysis of the 1300 UTC model output presented in the previous section is consistent with the existence of a sting jet leading to a low-level (about 850hPa) local wind maximum, and related enhanced 10m winds and gusts, together with an overrunning dry intrusion descending to about 750hPa, Lagrangian trajectory analysis provides conclusive identification of these wind jets through characterisation of their properties and paths. Lagrangian trajectories are calculated by following 'air parcels' backwards and/or forwards in time using suitably high temporal resolution model output. Here we use hourly model output and consider air parcels that begin at both 1300 and 1700 UTC (the times of the peaks in 850hPa wind speed in Figure 1b). As we are interested in the sources of the strong low-level winds at these times, trajectories are calculated from start points in a defined box (encompassing the strong low-level wind regions in the cold sector, as defined in the caption of Figure 4) and with wind speeds >49ms^{-1}; the precise values were chosen to focus on the intense core of the jets while providing a suitable number of trajectories. Trajectories were calculated using LAGRANTO (Sprenger and Wernli, 2015) and calculated backwards to 0000 UTC (on 1 November) and forwards for 2h from both start times. The relatively long backwards trajectory compared to the expected sting jet descent time of just a few hours has been chosen to also capture its characteristics prior to its descent and to strengthen the distinction between the dry intrusion and sting jet airstreams.

Maps similar to that shown in Figure 2(b) are shown every 3h from 0100 to 1300 UTC and then at 1700 UTC in Figure 4 with the addition of the instantaneous cyclone-relative positions of trajectories classified into four airstreams: two from each of the two starting times, according to their pressure value at 0000 UTC. The maps show the cyclone evolving from an open wave (Figure 4a) with strong 850hPa winds found only in the warm sector into a mature Shapiro–Keyser-type cyclone with the strongest winds found in the cold sector of the cyclone behind the fractured cold front (Figure 4f). Trajectories located above the 800hPa pressure level are coloured magenta and purple starting from 1300 and 1700 UTC, respectively, and those starting below this level are coloured cyan and blue for the same respective start times. This threshold pressure was chosen from consideration of the time-series of pressure, wind speed and
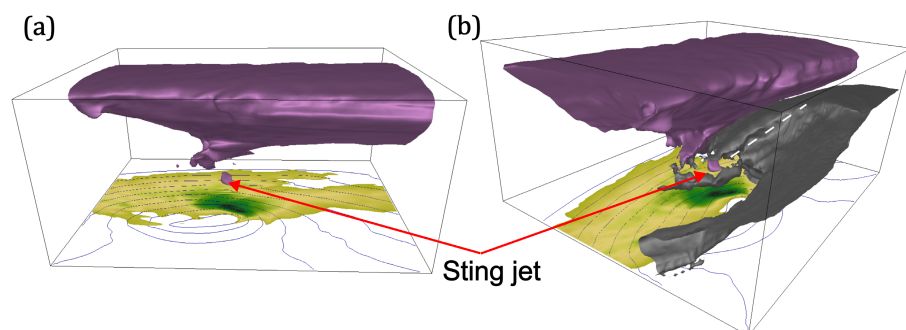

(a)   (b)

Sting jet

Figure 3. Three-dimensional renderings of the structure of Storm Ciarán *at 1300 UTC 1 November viewed from (a) the north and (b) the northeast of the storm. Box extends from 25 to 10°W and 40 to 52°N. Both panels show the 50ms^{-1} isosurface of wind speed (purple), as well as MSLP (blue contours every 4hPa down to 972hPa) and gusts (shading in yellow–blue from 25ms^{-1}; see Figure 2c for details) on the bottom surface. (b) also shows the 283.5K isosurface of θ_w (grey) with the axis of the valley in this field marked with a dashed white line. These plots were created using the VAPOR visualization and analysis platform (Li* et al.*, 2019; Visualization & Analysis Systems Technologies, 2023).*
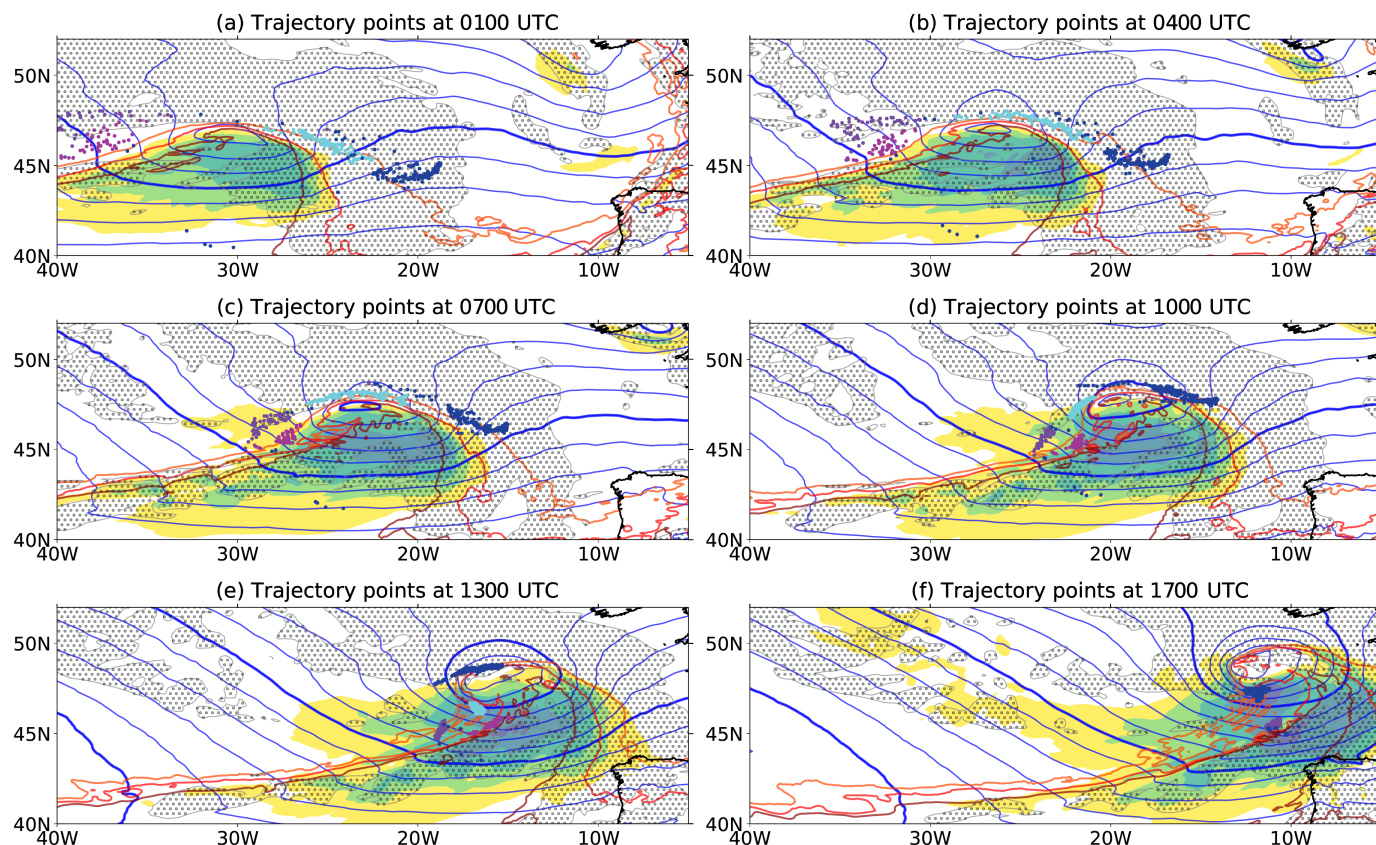
Figure 4. Sequence of maps for times during 1 November showing the low-level structure of Storm Ciarán *and the instantaneous location of trajectory points associated with the diagnosed airstreams leading to extreme cold sector winds: (a) 0100 UTC, (b) 0400 UTC, (c) 0700 UTC, (d) 1000 UTC, (e) 1300 UTC and (d) 1700 UTC. Shading and contours as in* Figure 2(b) *but with reduced opacity for the shading to improve the clarity of the overlying trajectory points. Trajectory points from trajectories starting at 1300 UTC are coloured cyan and magenta (not available in (f)) and those starting at 1700 UTC are coloured purple and blue; magenta and purple dots are for trajectories located above 800hPa at 0000 UTC and cyan and blue dots are for trajectories located below 800hPa at this time. All trajectories are between 775 and 925hPa (every 20hPa from 925hPa) with wind speeds >49ms⁻¹ at the start times with the starting points every 0.1° within (18.0–15.0°W, 45.0–47.5°N) at 1300 UTC and (14.0–9.0°W, 45.0–48.0°N) at 1700 UTC (inclusive). For the start times of 1300 and 1700 UTC, 165 and 230 trajectories, respectively, meet the criteria.*

relative humidity shown in Figure 5, which show that it distinguishes airstreams with distinct characteristics (the trajectory sets could have equally well been distinguished by thresholds in wind speed or relative humidity at the same time); no other criteria (e.g. on descent rate) have been applied here. The airstreams lying above and below the threshold pressure surface at 0000 UTC have the characteristics of the dry intrusion and sting jet, respectively.

The sting jet and dry intrusion airstreams are located in the strong wind regions equatorward of the bent-back front and above the surface (850hPa) cold front, respectively, at both start times (see the cyan and magenta dots in Figure 4e for 1300 UTC and the blue and purple dots in Figure 4f for 1700 UTC). The locations of the two airstreams for a given starting time diverge spatially going backwards in time (Figures 4a–d). The dry intrusion airstreams (purple and magenta) are located to the west of the developing cyclone at 0100 UTC (Figure 4a) and move fairly zonally towards the surface cold front. During this time they descend steadily by more than 100hPa and accelerate gently from a minimum wind speed of

about 30ms⁻¹ to the threshold wind speed (49ms⁻¹) over at least 10h (Figures 5a,b,d,e). These airstreams start relatively dry (relative humidity <60% and <20% at 0000 UTC for the trajectories with start times of 1300 and 1700 UTC, respectively) but moistening of some of the associated trajectories occurs as they approach the surface front, likely due to mixing with other airmasses (Figures 5c,f). In contrast, the sting jet airstreams (blue and cyan) are located in the cloud head ahead of the cyclone centre at 0100 UTC and track rearwards relative to the eastward moving cyclone as it intensifies, rotating around the cyclone centre to the tip of the cloud head before leaving the cloud head and descending into the frontal-fracture region (Figure 4). While in the cloud head, the instantaneous trajectory locations form a narrow band aligned with, and located on the polewards edge of, the tight frontal θ_w gradient. The sting jet airstreams begin in low-level cloudy air at 0100 UTC, ascend into the mid-troposphere (while staying cloudy) and then descend over just a few hours, during which time a large fraction of the trajectories undergo drying (Figures 5a,c,d,f). The sting jet airstreams have relatively low

wind speeds (≲20ms⁻¹) until about the time when they begin their descent when rapid acceleration occurs (Figures 5b,e). This is also about the time when the airstreams move into region of tight pressure gradient (associated with strong gradient wind speeds) to the south of the cyclone centre.

Comparing the two start times, the respective sting jet and dry intrusion airstreams have similar characteristics with the locations of the airstreams with the later start time located behind (in the airstream-direction sense) of those starting at the earlier start time throughout their evolution. However, there are some trajectories for the later start time that show transitional characteristics between those of the sting jet and dry intrusion airstreams and the sting jet airstream does not ascend as far before descending (up to at most about 750hPa compared to about 700hPa for the trajectories with the earlier start time). Figures 2(d) and 3 show how the small sting jet airstream is located beneath the much broader dry intrusion airstream and it is likely that the descending dry intrusion inhibits the level to which the sting jet airstream can ascend, prior to its descent, at later times.

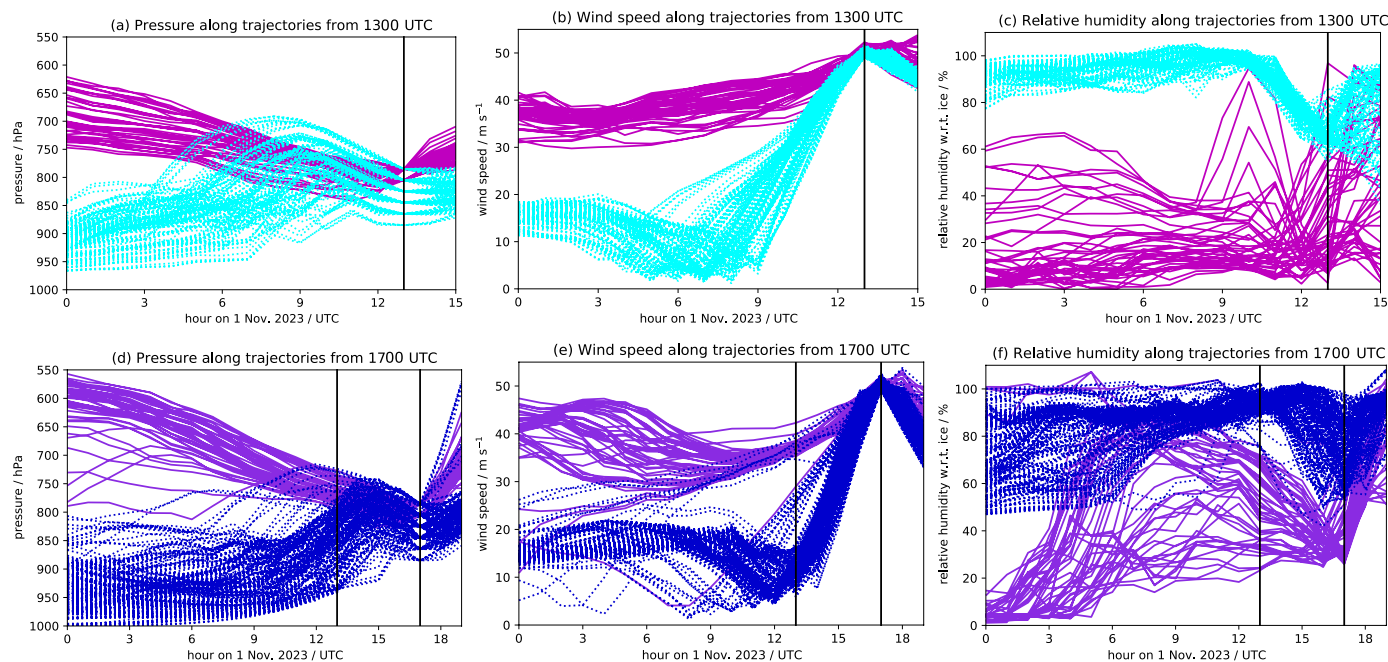**RMetS**
Royal Meteorological Society

Figure 5. Time-series of airstream characteristics along trajectories during 1 November: (a) pressure, (b) wind speed and (c) relative humidity with respect to ice for trajectories starting at 1300 UTC, (d–f) corresponding panels for trajectories starting at 1700 UTC. Vertical black lines mark 1300 and 1700 UTC. Trajectories are coloured as in Figure 4 with additionally different line styles used for the two different sets of trajectories in each panel (solid and dotted lines used for trajectories located above and below the 800 hPa level at 0000 UTC, respectively, such that the magenta and purple trajectories are dry intrusion airstreams and the cyan and blue trajectories are sting jet airstreams).
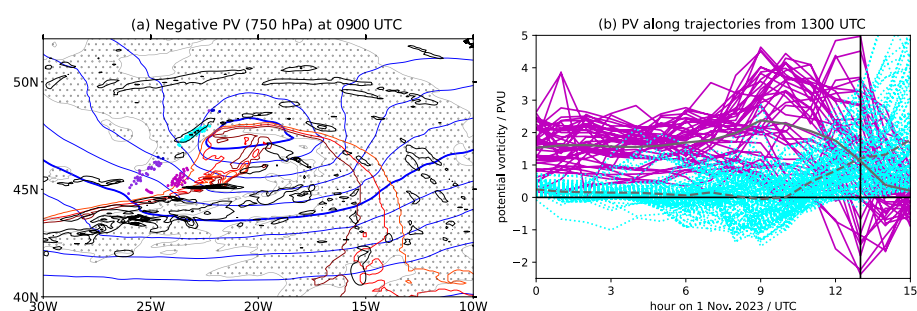

Figure 6. PV characteristics. (a) Horizontal map at 0900 UTC 1 November showing negative PV regions at 750 hPa (black contours every 1 PVU decreasing from 0 PVU); 850 hPa θ_w contours as in Figures 2(a–c), 750 hPa cloud denoted by stippling, and trajectories, and trajectory locations (as in Figure 4 but limited to those trajectories within 50 hPa of 750 hPa at this time). (b) Time-series of PV along trajectories during 1 November starting at 1300 UTC, vertical black lines marks 1300 UTC. Trajectories have the same colours and linestyles as in Figures 5(a–c). Mean trajectories are shown in grey (solid and dashed lines) for the dry intrusion and sting jet airstreams, respectively.

Evidence of mesoscale instability

Finally, we briefly consider evidence of mesoscale instability in the cloud head of Storm *Ciarán*. As described in Clark and Gray (2018), it is likely that a continuum of sting jet descent and speed-up mechanisms exists (see particularly their fig. 8). Mesoscale atmospheric instabilities, including conditional symmetric, inertial and symmetric instability, have been found in the cloud head tip of many published case studies of sting jet storms. Here, we analyse potential vorticity (PV) because regions of negative PV have a type of mesoscale instability termed symmetric instability. The presence of symmetric instability also

implies the presence of a moist variant of this instability termed conditional symmetric instability (where 'conditional' refers to the release of this instability being conditional on saturation, unlike for symmetric instability which is theoretically released as soon as it is generated); however, the inverse is not true, that is, not all regions with conditional symmetric instability also have symmetric instability. Symmetric instability has been found in the cloud heads of several intense sting jet storms (Volonté *et al.*, 2018, 2024b) as well as in idealised cases (Volonté *et al.*, 2020). A map showing regions of negative PV at 0900 UTC is shown in Figure 6(a) (this map is similar to those shown previously but including PV and with the wind speed omitted for clarity). This

time, and the pressure level of the PV field, is chosen based on Figure 5(a) to capture the sting jet associated with strong winds at 1300 UTC just prior to its descent: coloured dots show the location of the calculated trajectories at this time (as in Figure 4 but restricted to those that are close to the pressure level at which PV is shown). There is a lot of interesting negative PV structure in this map, particularly along the cold front. However, it is the elongated bands aligned with, and poleward of, the bent-back front that are relevant for the sting jet. Analysis of similar maps at different times reveals that these bands track cyclonically around the storm centre within the cloud head, towards the cloud head tip, with time (not shown). The sting jet airstream (cyan dots) is found within one of these bands at this time; the later descending sting jet airstream (i.e. with start points at 1700 UTC) only has a few trajectories at this level at this time, and so is not clearly visible and the dry intrusion airstreams are not found in negative PV regions.

The evolutions of PV along the sting jet and dry intrusion airstreams are distinct (Figure 6b). Although rather noisy (particularly for the dry intrusion airstream due to interpolation of the PV field to the trajectory locations in regions of strong PV gradients), the PV in the sting jet airstream decreases slightly prior to 0900 UTC, with many of the trajectories having negative PV, before increasing as the sting jet descends; this increase in PV implies that the associated symmetric instability is being released as the sting jet descends. In contrast the

PV of the dry intrusion airstream is substantially higher although the mean value decreases and a large spread in the values occurs after 0900 UTC, likely due to mixing (although with the caveat of possible errors due to interpolation). The evolution of PV in Storm *Ciarán* is thus consistent with the descent of its sting jet from the tip of the cloud head being enhanced by the release of mesoscale instabilities, including symmetric instability.

Conclusions

Sting jet(s) were speculated to exist in Storm *Ciarán* during its passage towards and over the United Kingdom on 1/2 November 2023 and in the immediate aftermath; for example, Manning and Fowler (2023) and Gray and Volonté (2023). Here the presence of two sting jet events has been evidenced by analysis of the storm's three-dimensional structure and airstreams calculated using Lagrangian trajectories using output from the Met Office global operational weather model. These events are associated with peaks in 850hPa wind speed exceeding 50ms^{-1} at 1300 and 1700 UTC on 1 November and the latter of these events was also associated with peaks in 10m wind speed and gusts (consistent with downward momentum transport through convective rolls or turbulent mixing). The sting jet is shown to be associated with a small region of strong winds extending downwards towards the surface, but with peak winds at about 850hPa, in the cold sector of the cyclone within the frontal fracture region equatorward of the cyclone centre. Another airstream, the dry intrusion, is also found to have contributed to strong winds, although at a much broader scale. At the time of the peak 850hPa winds, the peak winds associated with the dry intrusion were found aligned with and above the surface cold front, with peak winds extending down to about 875hPa. It is likely that these airstreams interact, particularly at the later time, such that the sting jet is limited in terms of its altitude prior to its descent towards the surface by the over-running dry intrusion. As in previously analysed case studies, the descent of the sting jet has been shown to be associated with the release of mesoscale instabilities; here we considered symmetric instability. This study provides further evidence of the importance of multiple, interacting airstreams in extreme cold sector winds, as previously demonstrated for storm *Eunice* from 2022 (Volonté *et al.*, 2024a,b).

Conflict of interest statement

The authors declare no conflicts of interest.

Author contributions

Suzanne L. Gray: Conceptualization; software; visualization; investigation; formal analysis; writing – original draft. **Ambrogio Volonté:** Conceptualization; writing – review and editing; investigation; formal analysis.

Data availability statement

No new datasets were created in this study. Operational forecast outputs used are archived at the Met Office; please contact the authors for details. Trajectory files can be provided upon request.

References

Browning KA, **Reynolds R**. 1994. Diagnostic study of a narrow cold-frontal rainband and severe winds associated with a stratospheric intrusion. *Q. J. R. Meteorol. Soc.* **120**: 235–257. https://doi.org/10.1002/qj.49712051602

Browning KA, **Roberts NM**. 1994. Structure of a frontal cyclone. *Q. J. R. Meteorol. Soc.* **120**: 1535–1557.

Charlton-**Perez AJ**, **Dacre HF**, **Driscoll S** *et al*. 2024. Do AI models produce better weather forecasts than physics-based models? A quantitative evaluation case study of Storm Ciarán. *npj Clim. Atmos. Sci.* **7**: 93. https://doi.org/10.1038/s41612-024-00638-w

Clark PA, **Gray SL**. 2018. Sting jets in extratropical cyclones: a review. *Q. J. R. Meteorol. Soc.* **144**: 943–969. https://doi.org/10.1002/qj.3267

Gray SL, **Volonté A**. 2023. Why Storm Ciarán's winds were so strong. https://theconversation.com/why-storm-ciarans-winds-were-so-strong-216923 (accessed 2 November 2023).

Hart NCG, **Gray SL**, **Clark PA**. 2017. Sting-jet windstorms over the North Atlantic: climatology and contribution to extreme wind risk. *J. Clim.* **30**: 5455–5471. https://doi.org/10.1175/JCLI-D-16-0791.1

Hewson TD, **Neu U**. 2015. Cyclones, windstorms and the IMILAST project. *Tellus A: Dyn. Meteorol. Oceanogr.* **67**: 27128. https://doi.org/10.3402/tellusa.v67.27128

Kendon M. 2023. Storm Ciarán, 1 to 2 November 2023. Technical report, Met Office. https://www.metoffice.gov.uk/weather/learn-about/past-uk-weather-events (accessed 17 May 2024).

Li S, **Jaroszynski S**, **Pearse S** *et al*. 2019. VAPOR: a visualization package tailored to analyze simulation data in earth system science. *Atmosphere* **10**: 488. https://doi.org/10.3390/atmos10090488

Manning C, **Fowler HJ**. 2023. Storm Ciarán is breaking records – and research suggests more severe weather in future. https://theconversation.com/storm-ciaran-is-breaking-records-and-research-suggests-more-severe-weather-in-future-216842 (accessed 2 November 2023).

Martínez-**Alvarado O**, **Baker LH**, **Gray SL** *et al*. 2014. Distinguishing the cold conveyor belt and sting jet air streams in an intense extratropical cyclone. *Mon. Weather Rev.* **142**: 2571–2595. https://doi.org/10.1175/MWR-D-13-00348.1

Met Office. 2024. National meteorological library and archive fact sheet 6 – the Beaufort scale. Technical report, Met Office. https://www.metoffice.gov.uk/research/library-and-archive/publications/factsheets (accessed 17 May 2024).

Rivière G, **Ricard D**, **Arbogast P**. 2020. The downward transport of momentum to the surface in idealized sting-jet cyclones. *Q. J. R. Meteorol. Soc.* **146**: 1801–1821. https://doi.org/10.1002/qj.3767

Sanders F, **Gyakum JR**. 1980. Synoptic-dynamic climatology of the 'bomb'. *Mon. Weather Rev.* **108**: 1589–1606.

Shapiro MA, **Keyser D**. 1990. Fronts, jet streams and the tropopause, in Extratropical Cyclones: The Erik Palmén Memorial Volume. Newton C, Holopainen EO (eds). American Meteorological Society: Boston, MA, pp 167–191.

Sprenger M, **Wernli H**. 2015. The LAGRANTO Lagrangian analysis tool – version 2.0. *Geosci. Model Dev.* **8**: 2569–2586. https://doi.org/10.5194/gmd-8-2569-2015

Visualization & Analysis Systems Technologies. 2023. Visualization and Analysis Platform for Ocean, Atmosphere, and Solar Researchers (VAPOR version 3.8.0). UCAR/NCAR – Computational and Information System Lab: Boulder, CO. https://doi.org/10.5281/zenodo.7779648 [Software].

Volonté A, **Clark PA**, **Gray SL**. 2020. Idealised simulations of cyclones with robust symmetrically unstable sting jets. *Weather Clim. Dyn.* **1**: 63–91. https://doi.org/10.5194/wcd-1-63-2020

Volonté A, **Gray SL**, **Clark PA** *et al*. 2024a. Strong surface winds in storm Eunice. Part 1: storm overview and indications of sting jet activity from observations and model data. *Weather* **79**: 40–45. https://doi.org/10.1002/wea.4402

Volonté A, **Gray SL**, **Clark PA** *et al*. 2024b. Strong surface winds in storm Eunice. Part 2: airstream analysis. *Weather* **79**: 54–59. https://doi.org/10.1002/wea.4401

Volonté A, **Clark PA**, **Gray SL**. 2018. The role of mesoscale instabilities in the sting-jet dynamics of windstorm Tini. *Q. J. R. Meteorol. Soc.* **144**: 877–899. https://doi.org/10.1002/qj.3264

Correspondence to: S. L. Gray
s.l.gray@reading.ac.uk

RMetS
Royal Meteorological Society